SANDIA REPORT

SAND2006-4864
Unlimited Release
Printed August, 2006

Impact of Polymer Film Thickness and Cavity Size on Polymer Flow during Embossing: Towards Process Design Rules for Nanoimprint Lithography

H. D. Rowland, W. P. King, A. C. Sun, and P. R. Schunk

Prepared by
Sandia National Laboratories
Albuquerque, New Mexico 87185 and Livermore, California 94550

Sandia is a multiprogram laboratory operated by Sandia Corporation,
a Lockheed Martin Company, for the United States Department of Energy's
National Nuclear Security Administration under Contract DE-AC04-94AL85000.

Sandia National Laboratories

Issued by Sandia National Laboratories, operated for the United States Department of Energy by Sandia Corporation.

Available to DOE and DOE contractors from
U.S. Department of Energy
Office of Scientific and Technical Information
P.O. Box 62
Oak Ridge, TN 37831

Telephone: (865) 576-8401
Facsimile: (865) 576-5728
E-Mail: reports@adonis.osti.gov
Online ordering: http://www.osti.gov/bridge

Available to the public from
U.S. Department of Commerce
National Technical Information Service
5285 Port Royal Rd.
Springfield, VA 22161

Telephone: (800) 553-6847
Facsimile: (703) 605-6900
E-Mail: orders@ntis.fedworld.gov
Online order: http://www.ntis.gov/help/ordermethods.asp?loc=7-4-0#online

SAND2006-4864
Unlimited Release
Printed August 2006

Impact of Polymer Film Thickness and Cavity Size on Polymer Flow during Embossing: Towards Process Design Rules for Nanoimprint Lithography

Harry D. Rowland[1], William P. King[1], Amy C. Sun[2], P. Randy Schunk[2]

[1]Woodruff School of Mechanical Engineering
Georgia Institute of Technology
Atlanta, GA 30329-0405

[2]Dept. 1514, Multiphase Transport Processes
Sandia National Laboratories
P.O. Box 5800
Albuquerque, New Mexico 87185-0836

Abstract

This paper presents continuum simulations of polymer flow during nanoimprint lithography (NIL). The simulations capture the underlying physics of polymer flow from the nanometer to millimeter length scale and examine geometry and thermophysical process quantities affecting cavity filling. Variations in embossing tool geometry and polymer film thickness during viscous flow distinguish different flow driving mechanisms. Three parameters can predict polymer deformation mode: cavity width to polymer thickness ratio, polymer supply ratio, and Capillary number. The ratio of cavity width to initial polymer film thickness determines vertically or laterally dominant deformation. The ratio of indenter width to residual film thickness measures polymer supply beneath the indenter which determines Stokes or squeeze flow. The local geometry ratios can predict a fill time based on laminar flow between plates, Stokes flow, or squeeze flow. Characteristic NIL capillary number based on geometry-dependent fill time distinguishes between capillary or viscous driven flows. The three parameters predict filling modes observed in published studies of NIL deformation over nanometer to millimeter length scales. The work seeks to establish process design rules for NIL and to provide tools for the rational design of NIL master templates, resist polymers, and process parameters.

Acknowledgments

The authors would like to thank Allen Roach for his help in developing meshed geometries and Tom Baer for his help in applying isolated boundary conditions.

Contents

Figures

Tables

Nomenclature

NIL	nanoimprint lithography
T_g	glass transition temperature
nm	nanometer
µm	micrometer
mm	millimeter
°C	degrees Celsius
X_o	characteristic length, tool width
P_o	characteristic pressure, applied load
T_o	characteristic time
U_o	characteristic speed
η	polymer viscosity
v^*	material dimensionless velocity
$v_m{}^*$	mesh dimensionless velocity
Γ^*	dimensionless fluid stress tensor
Re	Reynolds number
ρ	density
$\hat{n}$	normal vector
Ca	Capillary number
H^*	dimensionless curvature
$P_{rep}{}^*$	dimensionless repulsive force
d^*	dimensionless distance of the polymer boundary normal to the solid indenter
σ	surface tension
$\Gamma_s{}^*$	dimensionless elastic stress tensor
P^*	dimensionless body force of the embossing load
μ	Lame mu coefficient
λ	Lame lambda coefficient
E^*	dimensionless small deformation strain tensor
e^*	dimensionless small deformation volume strain
η_{inf}	infinite shear limit of polymer viscosity
η_o	zero shear limit of polymer viscosity
ω	polymer time constant
$\dot{\gamma}$	second invariant of shear rate tensor
n	shear thinning exponent
a	dimensionless parameter describing transition between low-rate and power-law
t	fill time
t_r	ramp time
S	indenter width
W	cavity half width
h_i	initial polymer film thickness
h_c	cavity height
t_h	half the time to onset of filling
t_o	time to onset of filling
t_f	time when polymer has covered half master cavity floor

h_r	residual film thickness
ΔP	pressure difference across the fluid interface
R_1, R_2	principal radii of curvature

1. Executive Summary

Nanoimprint lithography (NIL) is a high resolution, high-throughput, economical alternative to standard silicon based fabrication technologies. For NIL to become a viable manufacturing technology, a deep understanding of local polymer flow within simple geometries is required for rational process and master tool design.

This report presents continuum simulations of polymer flow during NIL, investigating the effects of imprint cavity geometry, polymer film thickness and properties, and process parameters. The simulations capture the underlying physics of polymer flow from the nanometer to millimeter length scale and examine geometry and thermophysical process quantities affecting cavity filling. Simulations investigate embossing of single rectilinear cavities of viscous dominant flows with no elastic stress relaxation, i.e. Reynolds number $<< 1$, Deborah number $<< 1$, and Capillary number $>> 1$. A uniform pressure applied to the silicon cavity presses the indenter into the viscous polymer film. No-slip conditions prescribed at the polymer-indenter and polymer-substrate interface model the contact while a capillary surface with surface tension captures the physics of the free polymer surface. Independent variation of imprint pressure, polymer viscosity, polymer film thickness, indenter width, and cavity width and height allows examination of parameters influencing local cavity filling time and polymer deformation mode.

Variations in embossing tool geometry during viscous flow distinguish different flow driving mechanisms. Three parameters predict polymer deformation mode: cavity geometry and polymer thickness ratio, polymer availability, and Capillary number. The ratio of cavity width to initial polymer film thickness defines the directional flow ratio, predicting the importance of deviatoric stress in determining single or dual peak deformation. Single peak flow is governed by the time required for the polymer to enter the cavity, while dual peak flow is governed by the time required for the indenter to penetrate the polymer. The ratio of indenter width to residual film thickness defines the polymer supply ratio, predicting the influence of squeeze flow and relative filling times independent of material rheological properties. Characteristic NIL Capillary number based on Stokes, squeeze, or single peak pipe flow fill time distinguishes between capillary or viscous driven flows, predicting flow driving mechanism to separate necessary process design from external embossing setup and internal material physics. The three parameters predict filling modes observed in published studies of NIL deformation over nanometer to millimeter length scales. The work seeks to establish process design rules for NIL and to provide tools for the rational design of NIL master templates, resist polymers, and process parameters.

2. Introduction

In nanoimprint lithography (NIL), a nanofabricated master tool having three-dimensional topography embosses a thermoplastic substrate, forming a negative relief of the master in the substrate. NIL offers scalable manufacture of nanoelectronics and nanoelectromechanical systems (NEMS) with resolution better than 10 nm [1] over areas greater than 1000 cm^2 [2]. Recent studies have improved NIL resolution below 5 nm [3] and to the molecular scale [4]. A deep understanding of polymer flow during NIL is critical for rational design of embossing tools and processes. This paper investigates viscous polymer flow during NIL for a wide range of master tool geometry and establishes a framework for NIL process design based on geometric ratios, polymer thickness, and Capillary number.

Several groups have investigated polymer flow during imprint lithography with different embossing geometries and length scales, resulting in several competing phenomenological models of polymer flow [5-11]. Experiments and simulations conducted from the millimeter to nanometer scale resulted in markedly different polymer deformation modes although length scale has not been the apparent cause of differentiation. Figure 1, showing single and dual peak viscous flow, illustrates two polymer deformation modes reported in NIL. Differences in deformation mode and replication fidelity have been attributed to a variety of factors, notably shear and extensional stretching, viscous flow and localized stress, residual stress release, shear-thinning and buckling, and surface tension.

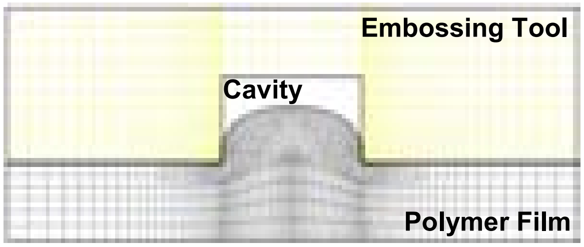

Single Peak

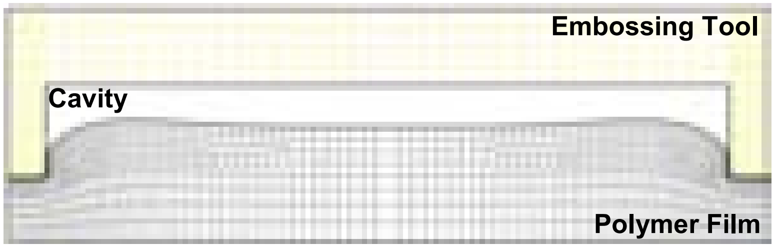

Dual Peak

Figure 1. Nanoimprint lithography polymer deformation modes, exhibiting either single or dual peak deformation.

Studies of embossing on the millimeter to micrometer scale have consistently cited the impact of shear deformation on replication while also noting other case-specific effects. Simulations and experiments at the millimeter scale [5] used a cavity of height 800 μm, width 3.5 mm, and spacing 3 mm to emboss a viscous PMMA film of thickness 1200 μm at 40 °C above its glass transition temperature (T_g). This system resulted in polymer flow with shear deformation at the mold surface and extensional stretching at the cavity center. Experiments at the micrometer scale [6] studied microembossing with indenter width 2 μm, cavity height 4 μm, and cavity widths 30 μm, 50 μm, and 100 μm and 15 – 20 μm thick PMMA films over a temperature range from T_g - 10 °C to T_g + 20 °C. A region of localized high strain occurred near the cavity sidewall, resulting in a deforming polymer peak that spread laterally and vertically to fill the cavity. The microembossing conditions resulted in viscous flow, localized stress, and shear-thinning phenomena dominant over surface tension effects. Indentation experiments at the micrometer to nanometer scale [7] pressed cylindrical micrometer sized cavities of height 2 μm and diameter 10 μm into glassy polymer films of thickness 450 nm and 1.7 μm. In the 450 nm film, the sharp cavity entrance produced extensive shear resulting in dual polymer peak filling. Indentation into the thicker films resulted in dual peak deformation for high loads and single peak deformation for low loads. Residual stress release on demolding influenced final replicated feature size, a phenomenon also noted in [12].

A few NIL studies investigated polymer deformation for film thicknesses and cavity heights in the 100 – 300 nm range. A large area flow experiment [8] studied cavity filling of 200 nm thick PMMA films embossed at T_g + 100 °C by cavities of width 20 μm, height 175 nm, and spacing 40 μm. The resulting deformation was a flat dual peak profile with vertical sidewalls and a central buckled region, attributed to effects from squeeze flow and shear-thinning at the indenter edge and compressive stresses in the interior of the cavity. This experimental work was followed by finite element simulations of a Newtonian fluid with surface tension [9]. These simulations showed the buckling region was the result of capillary forces acting over the large cavity width, where the polymer preferentially wetted the master surface. When surface tension effects were removed from the simulations, smooth single or dual peaks were observed dependent on cavity width, as observed in viscous flow experiments [6]. Other simulations and experiments [10, 11] investigated purely nanometer scale geometries and film thicknesses. Elastic solid simulations modeled the polymer with the nonlinear stress-strain behavior of a Moony-Rivlin material. The studies showed both single and dual peak flow confined near the master sidewall as described above [6, 7], and noted the effect of film thickness to retard deformation. The authors concluded that polymer in NIL shows rubber-like elastic dynamics above T_g with volume compression under high loads in thick polymer films, suggesting that the elastic component of polymers plays a large role in deformation even at temperatures well above T_g.

Simulations and experiments investigating embossing and imprint lithography from the millimeter to nanometer scale have yielded the common features of single or dual peak deformation that depends on a thermophysical property or process quantity. Each of the above-referenced studies offers a different phenomenological explanation of the observed behavior and there is little agreement about the relative importance of nonlinear elasticity, residual stress, linear and nonlinear viscous flow, compressive stresses, and capillary forces. There is a need for detailed and systematic study of geometric and material constraints over the length scales of interest. The lack of a comprehensive understanding of polymer flow in the 10 nm – 100 µm range limits NIL process design to ad-hoc or recipe-based approaches.

This paper presents simulations of liquid polymer deformation and filling modes during NIL under viscous-dominant conditions. Independent variation of imprint pressure, polymer viscosity, polymer film thickness, indenter width, and cavity width and height allows examination of parameters influencing cavity filling time and polymer deformation mode. A simple model of laminar flow between plates, Stokes flow, and squeeze flow characterizes the polymer filling time. The simulation regime is completely non-dimensionalized and the results are easily extrapolated for comparison to experiments investigating polymer flow in the 10 nm – 5 mm range. The simulation results predict behavior seen during all previously published NIL deformation studies. We suggest that three characteristic parameters, specifically, geometry ratios, polymer availability, and Capillary number, could form the nucleus of NIL process design rules.

3. Simulation Overview

Prior simulations of NIL have treated the polymer as either a viscous Newtonian fluid [9] or nonlinear elastic solid material [10, 11]. Solid mechanics simulations with a Moony-Rivlin constitutive model [10, 11] used the commercially-available MARC program, based on the finite element method and rectangular plane strain elements, to model the polymer as a rubber elastic above T_g. Fluid mechanics simulations [9] used the commercial computational fluid dynamics code CFD-ACE, based on the finite volume method, to simulate NIL on an Eulerian grid using the volume of fluid method (VOF) to track the deforming polymer interface. VOF methods have also been used to model micro injection molding [13, 14], but the methods sacrifice boundary shape accuracy for a faster speed of solution [15]. The free boundary or moving boundary simulations presented in this paper are ideally suited for *GOMA* [16], a Galerkin finite element program specialized for analysis of manufacturing flows having one or more transport fields such as those that exist in two-phase flows or for the freely-moving polymer surface of NIL.

GOMA allows the liquid polymer and the solid indenter to be treated in an arbitrary Langrangian/Eulerian (ALE) reference frame, thereby separating the polymer and solid motion from the mesh motion thus allowing for large free boundary deformations [15, 17]. All surfaces move as part of a fully-implicit, fully-coupled algorithm [15] that links the mesh motion to the material motion through surface kinematic conditions. A Newton-based solution algorithm enables the mesh motion and the rest of the problem physics to be solved simultaneously. For the simulations presented here, an implicit Backward-Euler time integration is used with a classical Gaussian elimination LU decomposition method. The maximum dimensionless time step size is 0.01 with a residual less than 10^{-7} at each time step. The mesh uses 9-node isoparametric quadrilaterals with smaller elements near the indenter-polymer interface and larger elements at the cavity center for accurate and swift solution convergence.

Figure 2 shows the finite element model with prescribed boundary conditions. The model assumes the embossing geometry is adequately vented or under vacuum conditions. To improve computation time and convergence, the problem is non-dimensionalized by choosing a characteristic length X_o equivalent to the tool width, pressure P_o equivalent to the applied load, time T_o equivalent to the ratio of polymer viscosity η to applied load, and speed U_o equivalent to the ratio of characteristic length to characteristic time. The characteristic time is chosen to match the timescale of microembossing experiments previously reported [6] and the characteristic speed is chosen to balance the viscous and pressure forces for computational ease. The scaled conservation equation for mass is

$$\nabla^* \cdot v^* = 0 , \tag{1}$$

and the scaled liquid momentum conservation equation is

$$Re\left(\frac{\partial v^*}{\partial t^*} + (v^* - v_m^*) \cdot \nabla^* v^*\right) = \nabla^* \cdot \Gamma^*, \tag{2}$$

where Re is the Reynolds number based on polymer zero shear viscosity, v^* and v_m^* are the material and mesh dimensionless velocity, respectively, and Γ^* is the dimensionless fluid stress tensor. The dimensionless Reynolds number is $\rho U_o X_o / \eta$, where ρ is the density.

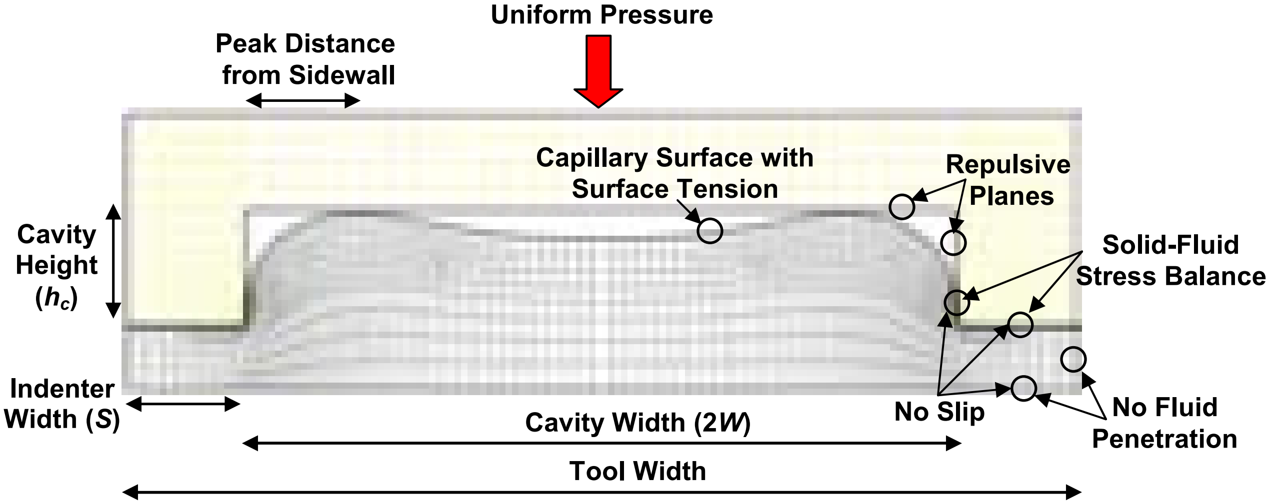

Figure 2. Nanoimprint lithography cavity and deforming polymer, showing simulation boundary conditions, geometry variables, and polymer peak deformation location measurement.

The boundary condition on the free surface of the liquid is modeled by a force balance of the fluid traction with capillary forces:

$$n \cdot \Gamma^* = \frac{1}{Ca} 2H^* n + \frac{1}{\eta U_o} \nabla_s^* \sigma + \frac{1}{X_o^4} \frac{P_{rep}^*}{d^{*4}}, \tag{3}$$

where n is the normal vector, Ca is the Capillary number, H^* is the dimensionless curvature, P_{rep}^* is an arbitrary dimensionless repulsive force, and d^* is the dimensionless distance of the polymer boundary normal to the solid indenter. The Capillary number $Ca = \eta U_o / \sigma$ is a ratio of viscous forces to surface tension forces, where σ is the surface tension. Equation 3 represents a force balance at the polymer-air interface that balances the surface tension force due to curvature of the surface, the gradient of surface tension along the surface, the normal stress from the fluid and the contact force due to the proximity of the solid surface. The contact force P_{rep}^* is not significant physically and is arbitrarily chosen to ensure no liquid penetration of the solid surface. The repulsive term is applied to the liquid surface normal to the contact plane, allowing the liquid to slip along the solid surface without penetrating the solid. The ALE framework allows the capillary boundary condition to define the material shape of the free surface and a kinematic mass balance condition ensures that the mesh location conforms to the material location at the boundary:

$$n \cdot (v^* - v_m{}^*) = 0\,. \tag{4}$$

The body of the liquid can still be represented by an immaterial mesh that does not introduce artificial sress or deformation while the capillary surface can determine the motion of the moving boundary. A no-slip condition is applied to the fluid at the initial fluid-solid interface with the indenter and substrate.

While the stress and strain in the solid master is important for NIL process design, the fluid deformation is of primary interest here so the simulations use a single solid cavity of small mass. Conservation of momentum transfers load from the solid to the fluid. Assuming elastic forces are much larger than inertial forces, solid momentum conservation is

$$\frac{1}{X_o}\nabla^* \cdot \Gamma_s^* + P_o P^* = 0\,, \tag{5}$$

where $\Gamma_s{}^*$ is the dimensionless elastic stress tensor and P^* is the dimensionless body force of the embossing load. The elastic stress tensor is

$$\Gamma_s = 2\mu E^* + \lambda e^* I\,, \tag{6}$$

where μ and λ are the Lame elastic coefficients, E^* is the dimensionless small deformation strain tensor, and e^* is the dimensionless small deformation volume strain. At the fluid-solid indenter interface, a stress balance is prescribed where the stresses in the fluid directly replace the stresses in the solid material residual equation at the interface. The balance in equation form is

$$\frac{P_o}{\mu} n \cdot \Gamma^* = n \cdot \Gamma_s^*\,. \tag{7}$$

GOMA is capable of modeling a variety of liquid constitutive equations. Both Newtonian fluid models and non-Newtonian Carreau-Yasuda models are used, where the Carreau-Yasuda model is given in unscaled form by

$$\eta = \eta_{\inf} + (\eta_o - \eta_{\inf})\left[1 + (\omega\dot{\gamma})^a\right]^{\frac{(n-1)}{a}}\,, \tag{8}$$

where η_{inf} and η_o are the infinite shear limit and zero shear limit viscosity, respectively, ω is the polymer time constant, $\dot{\gamma}$ is the second invariant of the shear rate tensor, n is the shear thinning exponent, and a is a dimensionless parameter describing the transition between the low-rate and power-law region. With proper constants, the model fits well the material properties described by Fuchs *et al* [18]. A Newtonian viscosity model better matches the time scale of microembossing experiments near T_g [6], hence a Newtonian material model is used for the majority of simulations.

To address the largest possible solution space, nondimensionalization reduces the number of simulation variables. Applied pressure P_o, polymer viscosity η, and initial film thickness h_i are chosen as the dimensional parameters, reducing the number of independent dimensionless variables to a dimensionless time to fill tP_o/η, ramp time t_rP_o/η, density $\rho P_o h_i^2/\eta^2$, indenter width or cavity spacing S/h_i, tool width $(2S+2W)/h_i$, and cavity height h_c/h_i. The fill time is t, the ramp time is t_r, the indenter width is S, the cavity half width is W, and the cavity height is h_c. Under viscous-dominant conditions, variations in density do not significantly influence the simulations. Ramp time is not thoroughly investigated for effects on shear rate. For a given applied pressure and polymer viscosity, the ratios of indenter width to film thickness, tool width to film thickness, and cavity height to film thickness are systematically varied to determine their effects on polymer deformation mode and time to fill. The dimensionless ramp time is constant for all cases.

4. Results

Simulations investigated polymer deformation during cavity filling for viscous-dominant conditions, i.e. $Re << 1$ and $Ca >> 1$, where the time scale of relaxation is less than the time scale of flow. Figure 2 shows a representative rectangular cavity having indenter width S, cavity height h_c, and cavity half width W. Of particular interest is the location and size of the polymer peak(s), and the time required to fill the cavity. Simulations modulated cavity geometry, polymer film thickness, and process conditions and examined their effect on polymer deformation mode. Most simulations modeled the polymer as a Newtonian fluid, but a few modeled the polymer as shear-thinning. Cylindrical cavities were briefly investigated as well.

4.1. Polymer Deformation Mode

Figure 3 shows the effect of rectangular cavity width and film thickness on polymer deformation, where dimensionless cavity size is the ratio of cavity width to tool width $W/(S+W)$ and dimensionless cavity height is the ratio of cavity height to film thickness h_c/h_i. The indenter width is constant and only the cavity width or polymer film thickness changes. For each configuration, deformation profiles are shown for four times: the start of imprinting t_i, half the time to onset of filling t_h, onset of filling t_o, and the time when polymer has covered half of the master cavity floor t_f. Onset of filling occurs when the polymer peak first touches the master cavity floor. As cavity width increases, the deformation mode changes from single peak to dual peak deformation. The polymer deformation also transitions from single to dual peak as the initial polymer film thickness decreases, as shown in Fig. 3b. For the largest cavity widths and thinnest polymer layers, the two peaks are highly localized near the vertical cavity walls and do not interact.

For all of the simulations of this paper, the polymer deformation occurs near the indenter sidewall. Figure 3c shows the transition from single to dual peak flow based on cavity half width W and initial film thickness h_i. The single to dual peak transition is clearly observed at W/h_i near 1.2. The polymer peak remains located roughly h_i from the indenter sidewall regardless of any other parameter. Small variations in peak location for a given value of W/h_i are due to polymer shear limits or complete cavity filling. The polymer peak will spread laterally but not indefinitely as the lateral motion of the peak is driven by shear near the indenter sidewall.

The degree of fluid shear-thinning behavior influences peak location, shown in Fig. 4. Deformation profiles are shown at a dimensionless time of 1.0 for a Newtonian fluid and shear-thinning fluids of varying degree, where η_{inf} and η_o differ by four orders of magnitude. A shear-thinning fluid of power law exponent 0.15 moves the polymer peak 10% closer to the sidewall than a Newtonian fluid and decreases the required time to fill by nearly 50% compared to the Newtonian fluid for this cavity. In general, a shear-dependent fluid will affect polymer flow where shear is greatest, which occurs for small indenter widths, large cavity widths, and small film thickness. The decrease in polymer shear modulus above T_g also promotes increased influence of shear-thinning parameters.

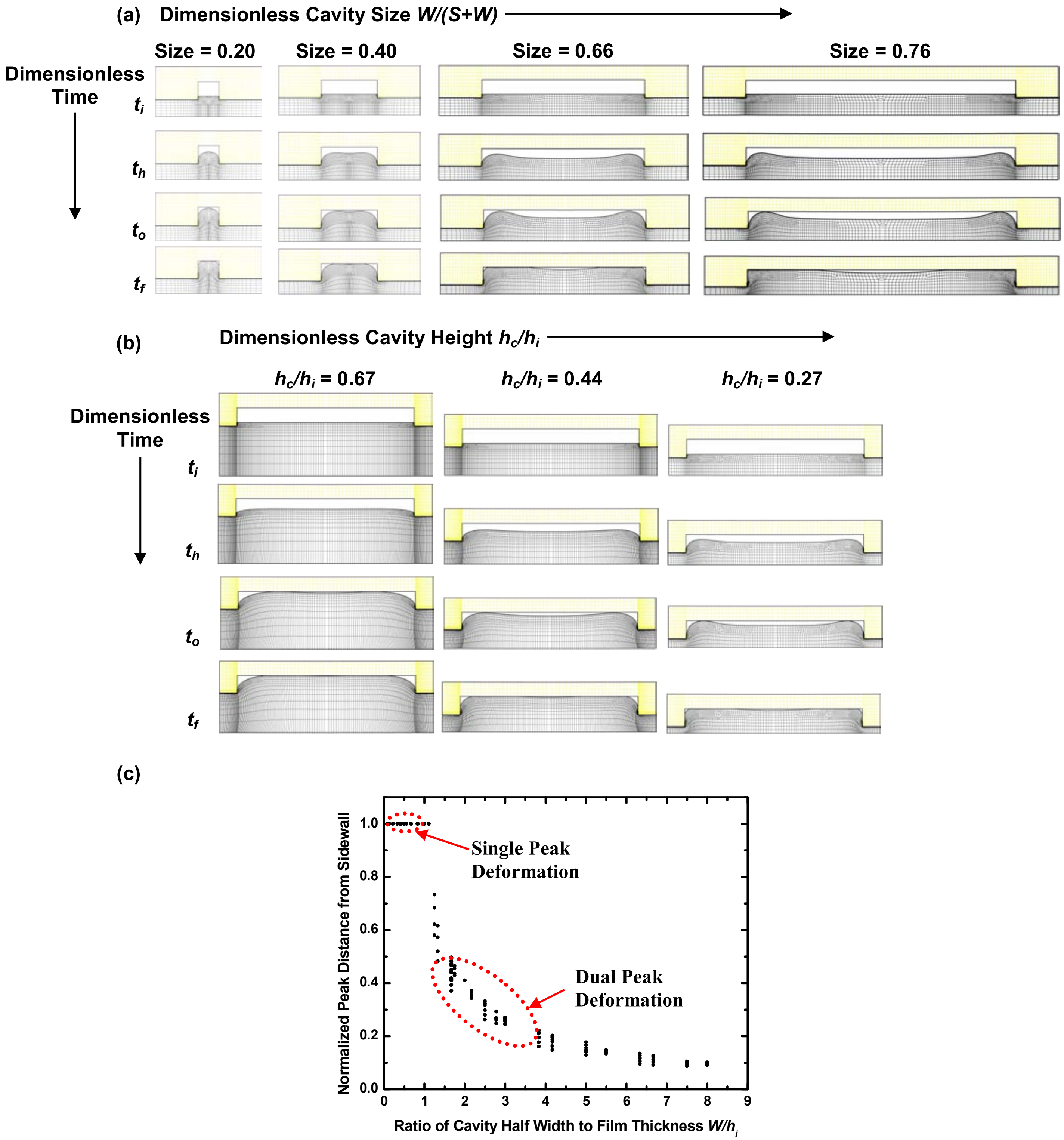

Figure 3. Deformation profiles for (a) increasing cavity width holding indenter width and film thickness constant and (b) decreasing film thickness holding cavity geometry constant. (c) Impact of resist film thickness on cavity filling. The location of the deforming polymer peak location is always a distance from the cavity vertical sidewall approximately equal to the polymer thickness.

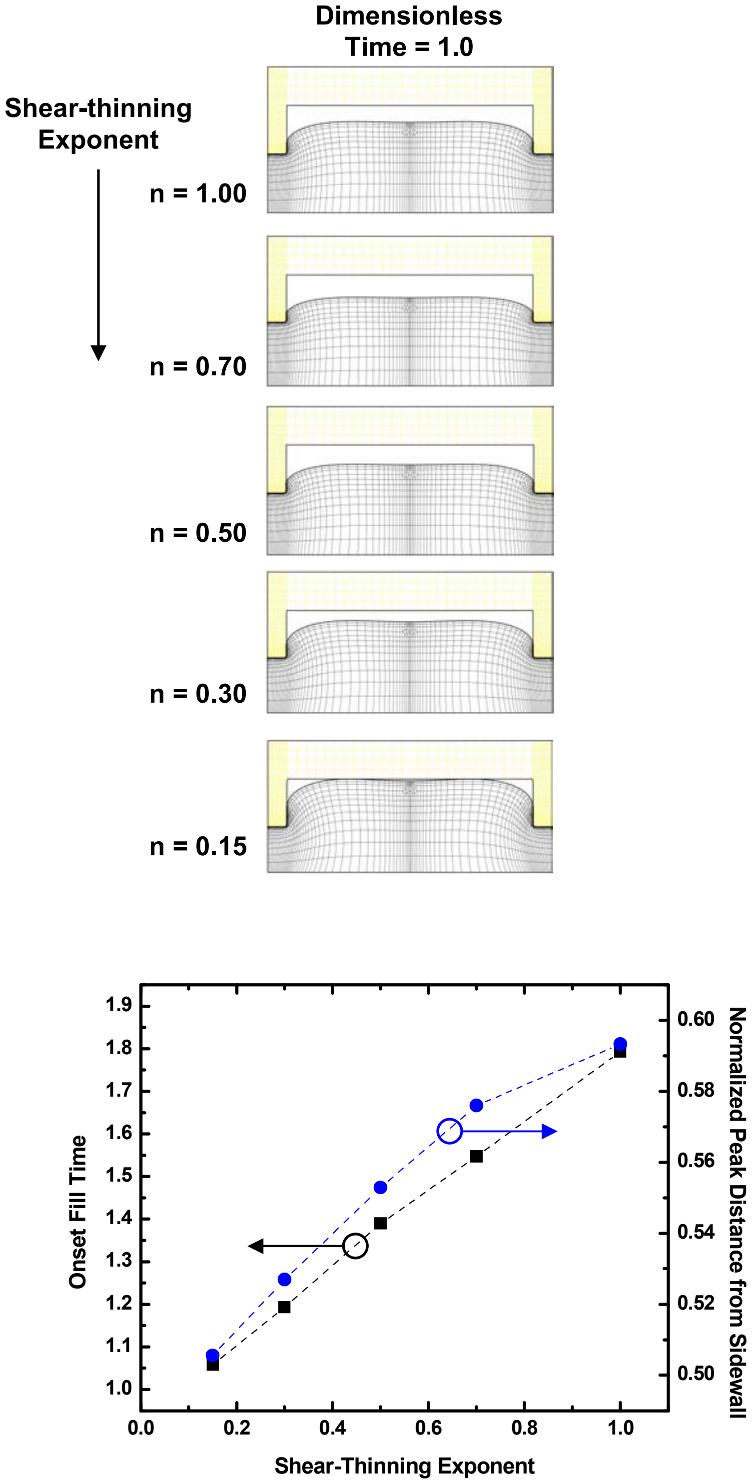

Figure 4. Effect of shear-thinning on deformation. Decreasing shear-thinning exponent from 1 (Newtonian) to 0.15 (highly shear-thinning) reduces the polymer viscosity near the vertical cavity wall, moving the polymer peak closer to the indenter sidewall and decreasing the time to fill.

The general trends of polymer flow are similar for cylindrical, as opposed to rectangular, embossing tools. Figure 5 compares Newtonian flow for a rectangular cavity and a cylindrical slot with equivalent cavity width and diameter. At $W/h_i = 1.4$, the cylindrical slot is in single peak deformation mode while the rectangular cavity deforms in a dual peak mode. Circumferential confinement in the cylindrical slot delays the transition from single to dual peak deformation to higher values of W/h_i. The cylindrical slot also requires longer time to fill than the rectangular cavity because of the same confinement.

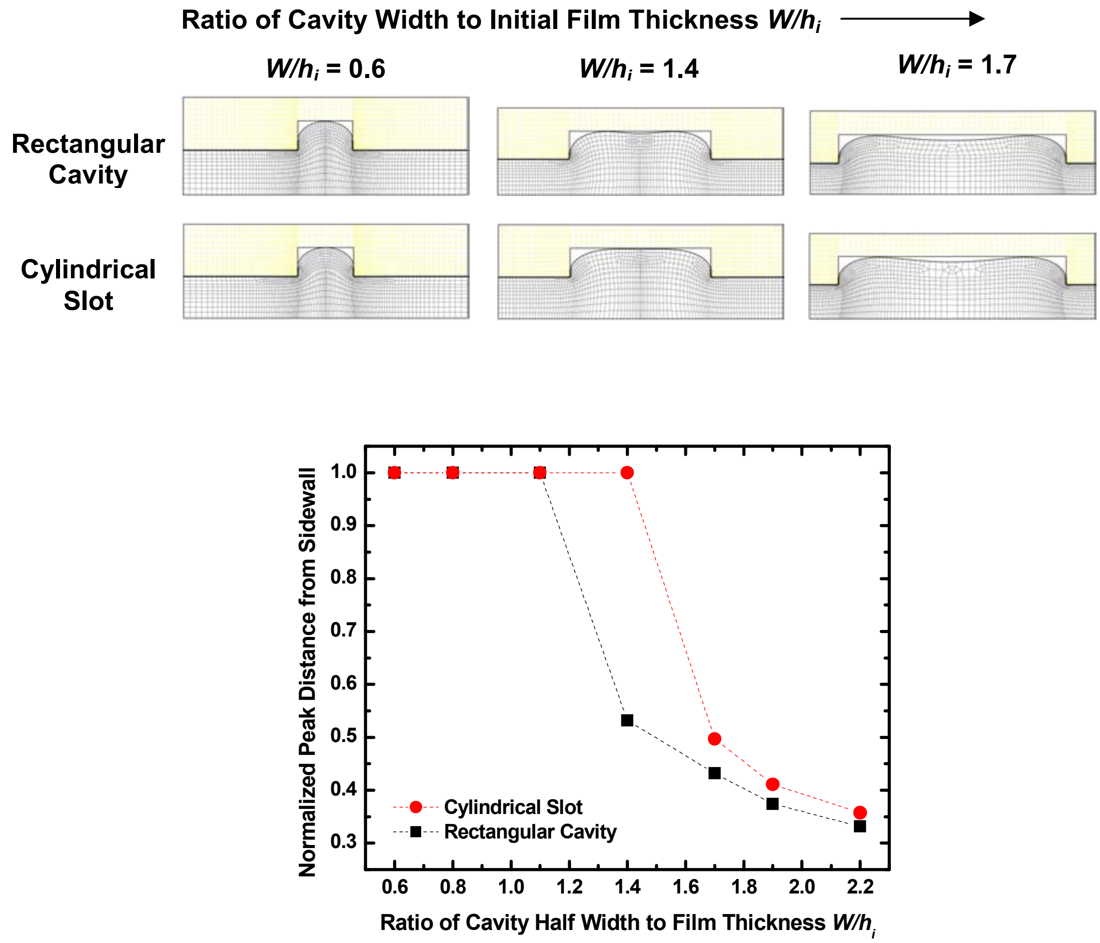

Figure 5. Comparison of geometric configuration for given cavity diameter or width. Confined geometry of a cylindrical slot delays the transition from single to double peak for increased cavity diameter. Cylindrical slot also requires longest time to fill.

4.2. Cavity Filling Times

Figure 6 shows the impact of rectangular cavity geometry and film thickness on fill times for a viscous Newtonian fluid, for several values of $W/(S+W)$ and constant $S+W$. In general, wider cavities fill faster than narrower cavities, and taller cavities on thin polymer films fill slower than shorter cavities on thick polymer films. In all cases, single vs. dual peak deformation mode affects cavity filling time, as the degree of shear in the polymer drives the filling. In both single and dual peak flow, it is possible to increase cavity width and/or decrease indenter width to promote shear. Figure 7 shows the effect of dimensionless cavity height on fill time. In general, taller cavities fill slower than shorter cavities. The wider cavities reach filling onset more rapidly than the narrower cavities but the overall filling time is not necessarily governed by cavity width. As Fig. 7 shows, once filling begins, the main restriction to polymer flow is not inside the cavity but between the indenter and the hard substrate, resulting in a squeeze flow. Figure 7b shows that squeeze flow in the polymer film becomes important as the indenter width S becomes greater than the residual film thickness h_r, i.e. when $S/h_r > 1$.

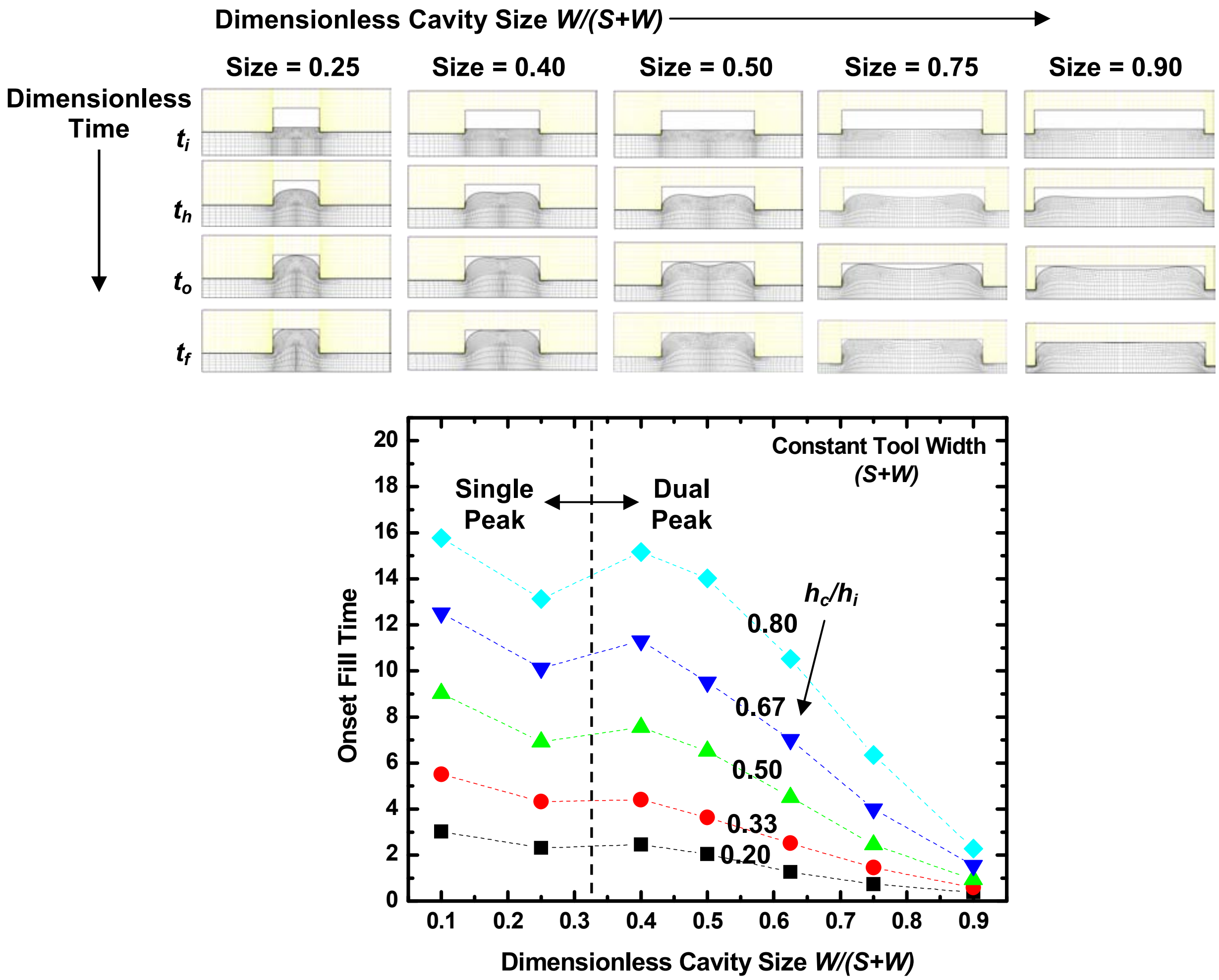

Figure 6. Impact of cavity size and cavity height to film thicknes ratio on cavity filling. Increasing cavity height to film thickness ratio increases time to fill. For both single and dual peak deformation, increasing the indenter width or decreasing the cavity size increases time to fill. Time to fill levels off at decreasing dimensionless cavity size as deformation transitions to single peak and begins to decrease for single peak flow. As cavity size continues to decrease, time to fill eventually increases dramatically as evenly distributed pressure forces polymer to travel thru confined slot.

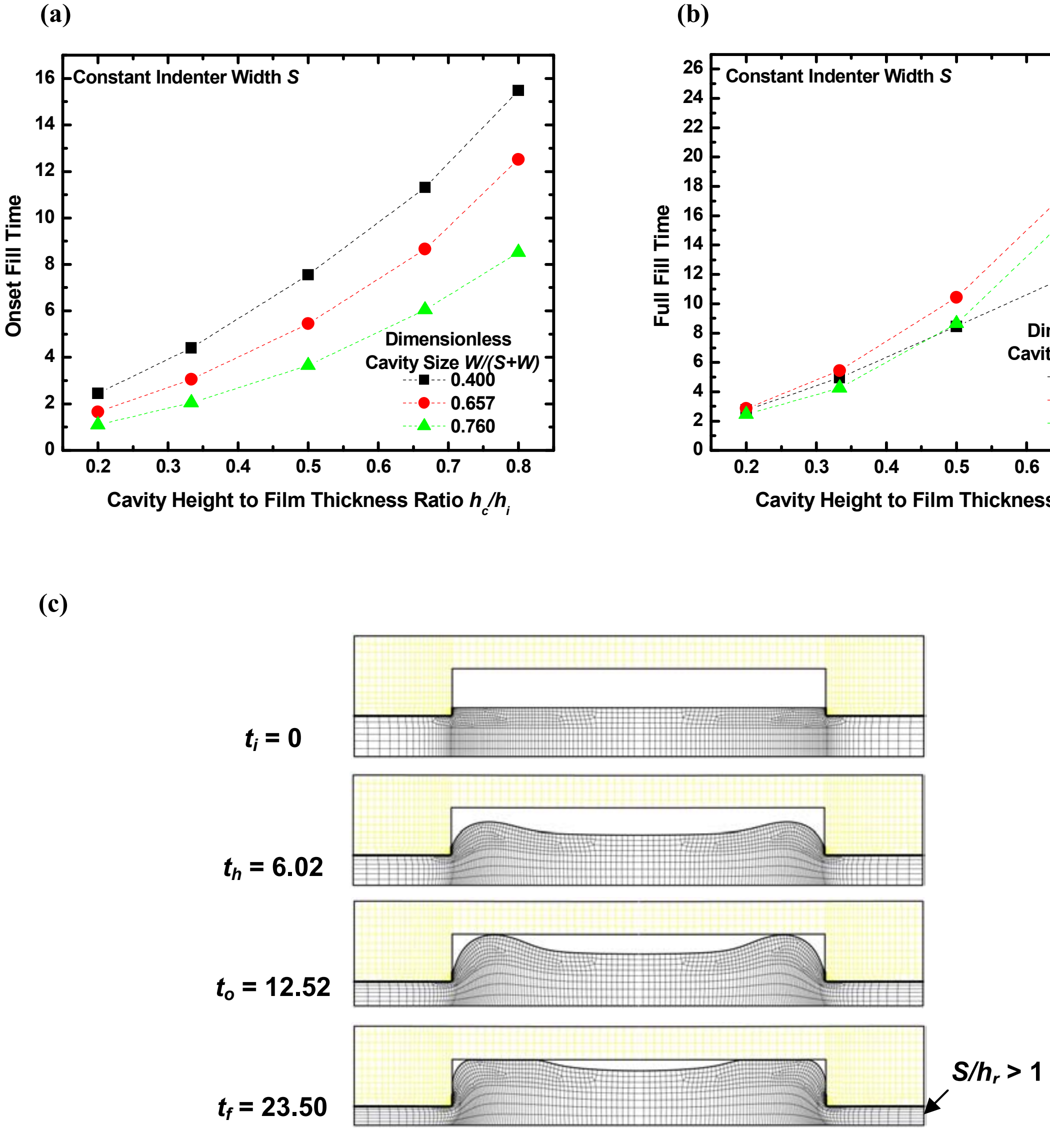

Figure 7. Impact of polymer availability on filling time. (a) Small cavity sizes require longest time to begin filling. (b) When the indenter width becomes greater than the residual film thickness, squeeze flow between the indenter and the substrate causes time to completely fill to dramatically increase. (c) Deformation profile showing the increasing time between fill onset and full filling.

5. Discussion

The polymer deformation predicted here agrees well with a number of articles that measure and model polymer deformation from the 10 nm to 1 mm scale. Nearly every report observed deforming polymer peaks located ~h_i from the master sidewall [5-7, 9-11, 19], with single peak deformation when the cavity half width was less than polymer film thickness, $W < h_i$, and dual peak deformation for cavity half width greater than polymer film thickness, $W > h_i$. The value W/h_i defined dual vs. single peak polymer deformation for measurements on films of thickness 1.2 mm [5], 500 μm [19], and 20 μm [6]. Experiments in 1.7 μm films [7] found single peak deformation at $W/h_i > 2$ while the present simulations predict dual peak deformation at $W/h_i > 1.2$, however the discrepancy can be attributed to stress relaxation following elastic rather than viscous deformation. Simulations that excluded surface tension examined embossing of 200 nm thick polymer films and produced single peak deformation for $W/h_i < 1$ and dual peak deformation for $W/h_i > 1$ [9]. The Newtonian liquid deformations presented here agree with nonlinear solid elastic deformations [10, 11] that also noted cavity geometry and initial film thickness modulate deformation mode.

The effects of film thickness and cavity geometry on filling time also agree well with reported values over a significant breadth of length scales. All of the referenced studies state that decreasing h_i or increasing h_c/h_i increases either the filling time [7, 8, 20] or the filling pressure [10, 11]. For the present viscous liquid simulations, time and pressure are linearly related in the non-dimensionalization. In solid mechanics simulations [11], both low and high aspect ratio structures required higher pressures to fill the cavity than intermediate aspect ratios. The present simulations agree with this previous finding and explain the phenomena by linking filling time to deformation mode, as shown in Figs. 6 and 7.

The ratio W/h_i accurately predicts single vs. dual peak deformation, indicating whether the polymer flow is mostly vertical or mostly lateral. As such W/h_i can be thought of as the *directional flow ratio*. Figure 8 shows contours of the mean shear rate (deviatoric shear stress) for three cavity widths on the same polymer film, for which there is single and dual peak deformation and free shear flow between the indenter and substrate, and also for dual peak flow and squeeze flow between the indenter and substrate. For the cases that there is no squeeze flow between the indenter and the substrate, there is a plug of non-deforming polymer in the cavity center. This plug is pushed upward in single-peak flow, but does not move in the case of dual peak flow, as it is too far from the indenter sidewall to be affected by the induced shear. When the polymer film between the indenter and substrate becomes thin, squeeze flow dominates the polymer filling, with consequences for filling time as well as deformation mode as illustrated in Fig. 7.

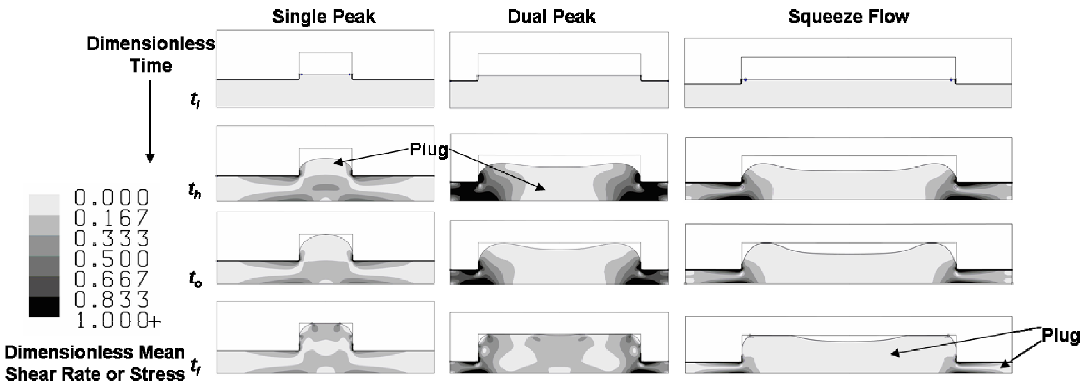

Figure 8. Mean shear rate or deviatoric stress profile. Single peak flow pushes non-shearing fluid plug vertically in a single polymer peak. Dual peak flow results from shear near the indenter sidewall with non-shearing fluid plug in cavity center. As flow transitions from shear dominant to squeeze dominant, a plug develops underneath the indenter as well as in the cavity center.

The three different characteristic flow profiles in Fig. 8 suggest cavity geometry governs filling behavior. Simple viscous flow theory, based on mold geometry ratios, can estimate a characteristic NIL filling time, t_{NIL}, for the filling of each geometry. The case of single peak flow, occuring when $W/h_i < 1$ regardless the value of S/h_r, resembles the classic fluid mechanics problem of steady laminar flow between infinite plates or within a pipe. Assuming fully developed flow and no slip conditions at the boundaries, a characteristic single peak pipe flow fill time can be defined as

$$t_{NIL} = \frac{12\eta h_c^{\,2} S}{P(2W)^2(S+W)} \tag{9}$$

and a characteristic velocity, V_{NIL}, may be found by dividing the distance the polymer must travel, i.e. the cavity height, by t_{NIL}:

$$V_{NIL} = \frac{P(2W)^2(S+W)}{12\eta h_c S}\,. \tag{10}$$

Fill times estimated by Eq. 9 correlate well with single peak fill times simulated here when $W/h_i < 0.5$. However, when $W/h_i > 0.5$, Eq. 9 underestimates simulated fill times by a factor of ~ 3 - 5. For these cases, simulated fill times seem to resemble flow through an abrupt expansion from a flow channel of h_i to $h_i + h_c$, resulting in roughly 60 - 80% head loss for the geometries simulated here [21]. Modifying Eq. 9 accounting for the expansion loss coefficient provides a better estimate for fill time when $0.5 < W/h_i < 1$. For the case of dual peak squeeze flow, when $W/h_i > 1$ and $S/h_r > 1$, the cavity filling time can be estimated by applying the lubrication approximation when assuming a fluid is squeezed out between infinite plates of width twice the indenter width moving at constant velocity due to an applied load. The situation of cavity filling in NIL cannot be accurately defined so simply since the polymer is expelled into a finite pressure field due to confinement and because the effective pressure decreases as more polymer comes into contact with the cavity surface, thus slowing the imprint. A reasonable characteristic squeeze flow filling time can be estimated as the time required to squeeze a fluid from the initial film thickness to the residual film thickness by infinite plates of width twice the tool width weighted by the ratio of indenter width to tool width:

$$t_{NIL} = \frac{\eta(S+W)^2}{2P}\left(\frac{1}{h_r^2} - \frac{1}{h_i^2}\right)\left(\frac{S}{S+W}\right). \tag{11}$$

This time is similar to the fill time defined by [8] but different by choice of plate width and weighting. Ignoring elastic effects, the residual film thickness h_r, or mold flash, is defined in terms of the master tool dimensions and initial polymer thickness

$$h_r = h_i - \frac{Wh_c}{S+W}. \tag{12}$$

A characteristic squeeze flow velocity can be found by dividing the difference in initial film thickness and residual film thickness by t_{NIL}: $V_{NIL}=(h_i-h_r)/t_{NIL}$. V_{NIL} is therefore

$$V_{NIL} = \frac{2P}{\eta S(S+W)}\frac{h_i^2 h_r^2}{h_i + h_r}. \tag{13}$$

This velocity is close to the imprint velocity defined by [9] but again different by choice of plate width and weighting. The squeeze flow characteristic fill time best approximates simulated fill times at large W/h_i when the polymer squeezed from beneath the indenter meets low pressure resistance in the cavity center. For dual peak shear free flow when $W/h_i > 1$ and $S/h_r < 1$, a different characteristic fill time may be defined based on Stokes flow [22]. Like squeeze flow filling, shear flow filling will be slowed as more polymer contacts the cavity surface. Hence a practical estimate for a characteristic Stokes fill time can be defined using the tool width, rather than the indenter width, as the indenting surface, giving

$$t_{NIL} = \frac{6\eta}{P(S+W)}(h_i - h_r), \tag{14}$$

and a corresponding characteristic Stokes velocity of

$$V_{NIL} = \frac{P(S+W)}{6\eta}. \tag{15}$$

Regardless of length scale, directional flow ratio W/h_i and polymer supply ratio S/h_r can determine appropriate V_{NIL}, which in turn can define a Capillary number characteristic of the imprint process, $Ca_{NIL}=\eta V_{NIL}/\sigma$. From Eqs. 10, 13, and 15, the viscosity dependence of V_{NIL} eliminates the viscosity dependence of Ca_{NIL}.

Three parameters, Ca_{NIL}, W/h_i, and S/h_r, can predict all of the previously reported polymer deformation modes during NIL. Ca_{NIL} determines viscous vs. capillary driven flow, the directional flow ratio W/h_i predicts single or dual peak flow, and the polymer supply ratio S/h_r determines shear-dominant Stoke's flow vs. squeeze flow. Table 1 lists imprint parameters from a number of articles that examined polymer flow during embossing and also lists Ca_{NIL}, W/h_i, and S/h_r. Figure 9 shows two regime maps of polymer filling modes and plots the simulations and experiments listed in Table 1. Figure 9a shows the determination of V_{NIL} from W/h_i and S/h_r and Fig. 9b shows flow driving mechanism defined by W/h_i and Ca_{NIL}. When located on the regime maps of Fig. 9, all of the experiments and simulations of Table 1 fall within their region of reported flow behavior. For the present simulations and the viscous deformation measurements of cited references [5-7, 19], the single vs. dual peak deformation is independent of capillary number and is determined by geometry only. A cylindrical slot can shift the transition from single to dual peak deformation to a higher value of W/h_i than occurs in rectilinear cavities.

Table 1. Comparisons of millimeter, micrometer, and nanometer scale imprinting. All studies are for negligible Reynolds number flows ($Re < 10^{-14}$). Using a characteristic velocity derived from viscous flow theory, all different flow regimes reported may be characterized by capillary number and geometry ratios. The NIL capillary number is independent of viscosity.

Experiment	h_r (nm)	h_r/h_i	**W/h_i**	**S/h_r**	V_{NIL} (nm/sec)	**Ca_{NIL}**	Flow Profile
Rowland [6]	5.67×10^{3}	63.0%	**1.11**	**0.35**	6.00×10^{1}	**2.02×10^{3}**	Single Peak Viscous
Rowland [6]	5.30×10^{3}	58.8%	**2.78**	**0.38**	1.35×10^{2}	**4.55×10^{3}**	Dual Peak Viscous
Rowland [24]	2.67×10^{3}	44.4%	**4.17**	**1.88**	1.18×10^{1}	**3.98×10^{2}**	Dual Peak Viscous Squeeze
Heyderman [8]	1.56×10^{2}	78.1%	**50.0**	**192**	5.48×10^{0}	**5.54×10^{-4}**	Dual Peak Capillary Squeeze
Jeong [9]	1.94×10^{2}	97.2%	**2.50**	**77.2**	3.96×10^{1}	**3.99×10^{-3}**	Dual Peak Capillary Squeeze
Jeong [9]	1.99×10^{2}	99.7%	**0.25**	**75.2**	5.73×10^{3}	**5.79×10^{-1}**	Dual Peak Capillary-Viscous Squeeze or Confined Single Peak (Wet-dependent)
Cross [7]	1.29×10^{3}	75.7%	**2.94**	**4.66**	9.83×10^{-1}	**3.31×10^{1}**	Dual Peak Viscous
Cross [7]	1.29×10^{3}	75.7%	**2.94**	**4.66**	7.45×10^{0}	**2.51×10^{2}**	Dual Peak Viscous
Cross [7]	3.68×10^{1}	8.2%	**11.1**	**163**	1.74×10^{-4}	**5.85×10^{-3}**	Dual Peak Capillary Squeeze
Hirai [10]	-1.5×10^{1}	-12.5%	**4.17**	**-33.3**	3.70×10^{-4}	**1.25×10^{-1}**	Dual Peak Capillary-Viscous Squeeze
Hirai [10]	1.15×10^{2}	46.0%	**2.00**	**4.35**	2.72×10^{-2}	**9.15×10^{0}**	Dual Peak Viscous-Capillary Squeeze
Hirai [10]	2.25×10^{2}	62.5%	**1.39**	**2.22**	1.35×10^{-1}	**4.53×10^{1}**	Dual Peak Viscous
Juang [5]	6.40×10^{5}	53.3%	**2.92**	**2.34**	5.98×10^{3}	**2.01×10^{4}**	Dual Peak Viscous
Shen [19]	4.50×10^{5}	90.0%	**0.20**	**0.22**	1.20×10^{2}	**4.04×10^{3}**	Confined Single Peak Viscous
Austin [3]	9.50×10^{1}	95.0%	**0.07**	**0.07**	3.43×10^{-1}	**1.15×10^{-2}**	Confined Single Peak Capillary (Non-wetting)
Yu [25]	4.64×10^{1}	22.1%	**1.07**	**7.01**	2.11×10^{0}	**7.10×10^{-2}**	Single Peak Capillary (Non-wetting)

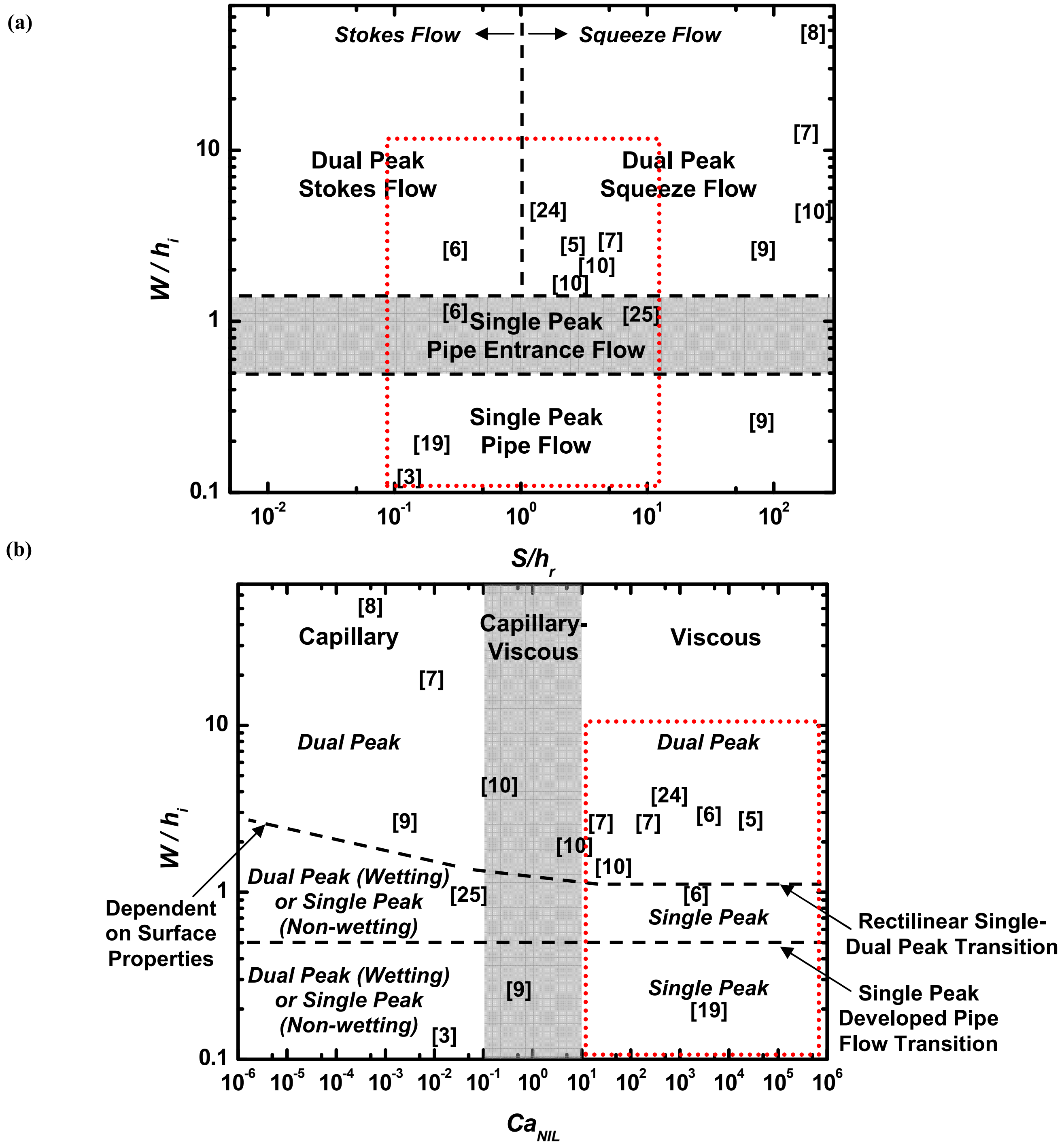

Figure 9. NIL polymer deformation regime maps for NIL capillary number Ca_{NIL}, directional flow ratio W/h_i, and polymer supply ratio S/h_r. All of the NIL flows reported in the reference of Table 1 are located on the maps, and fall into the polymer flow regime predicted by the theory of the present paper. The dotted square indicates the simulation space of this work. (a) Directional flow ratio and polymer availability determine characteristic velocity governing polymer deformation. (b) The effect of cavity geometry and polymer film thickness on polymer deformation. Ca_{NIL} governs viscous vs. capillary flow, and W/h_i governs single vs. dual peak polymer deformation.

Surface tension can influence the single to dual peak transition in capillary flows. As capillary forces become significant relative to viscous forces, the transition from single to dual peak deformation can occur at higher values of W/h_i than in purely viscous flow as the surface forces act to minimize the polymer surface area. The region where viscous forces are comparable to capillary forces is shaded in Figure 9. Competing viscous and capillary forces can explain the flat deformation profile resulting from a wetting fluid filling a thin cavity observed by [9]. In the strictly capillary region, transition from single to dual peak deformation depends strongly on surface chemistry. For a wetting fluid having a small contact angle with the master sidewall, the fluid will wet the master surface and climb the indenter sidewalls in a dual peak mode, independent of W/h_i. This wetting behavior has been observed by [8, 9, 20]. The deformation behavior for a non-wetting fluid is more complex than for a wetting fluid, and can depend on surface tension, contact angle, viscosity, pressure, film thickness, and cavity spacing. For a non-wetting fluid with large contact angle, polymer flow will be governed by the ratio of pressure and surface tension. The classical form of the Young-Laplace equation relates the radius of curvature of a fluid surface with the surface tension:

$$\Delta P = \sigma\left(\frac{1}{R_1} + \frac{1}{R_2}\right), \tag{13}$$

where ΔP is the pressure difference across the fluid interface and R_1 and R_2 are the principal radii of curvature. For a surface confined in only one direction, R_1 is finite while R_2 is infinite. The range of surface tension values for common engineering materials spans only 1-2 orders of magnitude [21] and thus for a given cavity, changes in embossing pressure will affect the curvature of the deforming polymer. While in the viscous regime, W/h_i alone modulates single to dual peak transition, for a non-wetting fluid in capillary flow, the single to dual peak transition also depends on surface tension and contact angle, and in general occurs at larger W/h_i. Furthermore, for a non-wetting fluid capillary flow, the impact of cavity curvature is more important than for rectangular cavities, and thus single to dual peak transition in a cylindrical cavity is shifted to higher W/h_i than for a rectilinear cavity.

The three parameters W/h_i, S/h_r, and Ca_{NIL}, can guide NIL process design. The directional flow ratio W/h_i distinguishes between vertical and lateral mold filling, which is important for replicating smooth surfaces of unfilled cavities as in the NIL manufacture of optics components. The polymer supply ratio S/h_r gauges the tradeoff between relative filling time and residual film thickness. The residual film thickness is critical for nanoelectronics fabrication where the mold flash must be removed before further processing. High values of the polymer supply ratio may also be unattainable in glassy or glass-like polymer systems [7, 23]. Ca_{NIL} determines the dominant flow driving mechanism in NIL and defines the imprint regimes where surface chemistry must be considered. In the viscous regime, modulating polymer viscosity through pressure or temperature can improve replication time.

6. Conclusions

This paper performs simulations of viscous polymer flow during nanoimprint lithography, investigating the effects of imprint cavity geometry, polymer film thickness and properties, and process parameters. Polymer deformation and fill time is governed by location and rate of polymer shear during imprinting, exhibiting deformation predominantly close to the vertical indenter sidewall that can result in single peak or dual peak deformation modes. The continuum simulations capture the NIL physics observed by numerous published articles from the 10 nm to 1 mm scale.

Three parameters, W/h_i, S/h_r, and Ca_{NIL}, accurately predict polymer deformation and filling mode. The directional flow ratio W/h_i predicts importance of deviatoric stress determining single or dual peak deformation and hence vertical or lateral flow. The polymer supply ratio S/h_r predicts the influence of squeeze flow and relative filling times independent of material rheological properties. The NIL Capillary number, Ca_{NIL}, predicts flow driving mechanism to distinguish necessary process design from external embossing setup and internal material physics. The three parameters W/h_i, S/h_r, and Ca_{NIL} combine to allow rational and predictive NIL process design and provide a step towards establishing design rules for NIL. Rather than rely on improvised trial and error, it is possible to use these tools to appropriately tailor tool geometry, process conditions, and polymer rheology and surface chemistry for optimal NIL.

7. References

1. Chou, S. and P. Krauss, *Imprint lithography with sub-10 nm feature size and high throughput.* Microelectronic Engineering, 1997. **35**: p. 237-240.
2. Khang, D. and H. Lee, *Wafer-scale sub-micron lithography.* Applied Physics Letters, 1999. **75**: p. 2599-2601.
3. Austin, M.D., et al., *Fabrication of 5 nm linewidth and 14 nm pitch features by nanoimprint lithography.* Applied Physics Letters, 2004. **84**(26): p. 5299-5301.
4. Hua, G., et al., *Polymer Imprint Lithography with Molecular-Scale Resolution.* Nano Letters, 2004. **4**(12): p. 2467-2471.
5. Juang, Y.-J., L.J. Lee, and K.W. Koelling, *Hot Embossing in Microfabrication. Part II: Rheological Characterization and Process Analysis.* Polymer Engineering and Science, 2002. **42**(3): p. 551-566.
6. Rowland, H.D. and W.P. King, *Polymer deformation and filling modes during microembossing.* Journal of Micromechanics and Microengineering, 2004. **14**: p. 1625-1632.
7. Cross, G.L.W., et al., *The Mechanics of Nanoimprint Forming.* Materials Research Society Symposium Proceedings, 2004. **841**.
8. Heyderman, L.J., et al., *Flow behaviour of thin polymer films used for hot embossing lithography.* Microelectronic Engineering, 2000. **54**: p. 229-245.
9. Jeong, J.-H., et al., *Flow Behavior at the Embossing Stage of Nanoimprint Lithography.* Fibers and Polymers, 2002. **3**(3): p. 113-119.
10. Hirai, Y., et al., *Study of the resist deformation in nanoimprint lithography.* Journal of Vacuum Science and Technology B, 2001. **19**(6): p. 2811-2815.
11. Hirai, Y., et al., *Simulation and experimental study of polymer deformation in nanoimprint lithography.* Journal of Vacuum Science and Technology B, 2004. **22**(6): p. 3288-3293.
12. Martin, C., L. Ressier, and J.P. Peyrade, *Study of PMMA recoveries on micrometric patterns replication by nano-imprint lithography.* Physica E, 2003. **17**: p. 523-525.
13. Haagh, G.A.A.V. and F.N. Van De Vosse, *Simulation of Three-Dimensional Polymer Mould Filling Processes using a Pseudo-Concentration Method.* International Journal for Numerical Methods in Fluids, 1998. **28**: p. 1355-1369.
14. Pitchumani, R., et al. *Analysis of a Process Replication of Electroforming Molds with Integral Microscreens*. in *Micromachining and Microfabrication Process Technology IX*. 2004. San Jose, CA: Proceedings of SPIE.
15. Sackinger, P.A., P.R. Schunk, and R.R. Rao, *A Newton-Raphson Pseudo-Solid Domain Mapping Technique for Free and Moving Boundary Problems: A Finite Element Implementation.* Journal of Computational Physics, 1996. **125**: p. 83-103.
16. Schunk, P.R., et al., *Goma 4.0- A Full-Newton Finite Element Program for Free and Moving Boundary Problems with Coupled Fluid/Solid Momentum, Energy, Mass, and Chemical Species Transport: User's Guide*. 2002, Sandia National Laboratories.

17. Schunk, P.R., *TALE: An Arbitrary Lagrangian-Eulerain Approach to Fluid-Structure Interaction Problems*, in *Sandia Technical Report*. 1999 (unpublished), Sandia National Laboratories.
18. Fuchs, K., C. Friedrich, and J. Weese, *Viscoelastic Properties of Narrow-Distribution Poly(methyl methacrylates).* Macromolecules, 1996. **29**: p. 5893-5901.
19. Shen, X.J., L.-W. Pan, and L. Lin, *Microplastic embossing process: experimental and theoretical characterizations.* Sensors and Actuators A, 2002. **97-98**: p. 428-433.
20. Scheer, H.C. and H. Schulz, *A contribution to the flow behaviour of thin polymer films during hot embossing lithography.* Microelectronic Engineering, 2001. **56**: p. 311-332.
21. Fox, R.W. and A.T. McDonald, *Introduction to Fluid Mechanics*. 5th ed. 1998, New York: John Wiley & Sons, Inc. 762.
22. Deen, W.M., *Analysis of Transport Phenomena*. Topics in Chemical Engineering, ed. K.T. Gubbins. 1998, New York: Oxford University Press. 597.
23. Cross, G.L.W., B.S. O'Connell, and J.B. Pethica, *Influence of Elastic Strains on the Mask Ratio in Glassy Polymer Nanoimprint.* Applied Physics Letters, 2004 (submitted).
24. Rowland, H.D., et al., *This paper.*
25. Yu, Z., H. Gao, and S.Y. Chou, *In situ real time process characterization in nanoimprint lithography using time-resolved diffractive scatterometry.* Applied Physics Letters, 2004. **85**(18): p. 4166-4168.

Distribution:

1	MS9004	Jill Ruby	08100
1	MS0824	Wahid Hermina	01510
1	MS0836	Pat Notz	01514
1	MS0836	Rekha Rao	01514
1	MS9161	Bob Nilson	08764
1	MS0834	Anne Grillet	01512
1	MS0834	Carlton Brooks	01512
1	MS0834	Chris Bourdon	01512
1	MS1245	John Emerson	02453
2	MS9018	Central Technical Files	8944
2	MS0899	Technical Library	4536
1	MS0123	D. Chavez, LDRD Office	1011
1	MS0115	CRADA Administration	1323
1	MS0161	Patent and Licensing Office	11500